Korean J. Chem. Eng., 35(6), 1263-1273 (2018)
DOI: 10.1007/s11814-018-0032-x

pISSN: 0256-1115
eISSN: 1975-7220

Kinetic models of Fischer-Tropsch synthesis reaction over granule-type Pt-promoted Co/Al_2O_3 catalyst

Hyun Mo Koo*, Myung June Park,†, Dong Ju Moon***, and Jong Wook Bae*,†**

*School of Chemical Engineering, Sungkyunkwan University (SKKU),
2066 Seubu-ro, Jangan-gu, Suwon, Gyeonggi-do 16419, Korea
**Department of Energy Systems Research, Ajou University, Suwon, Gyeonggi-do 16499, Korea
***Clean Energy Chemical Engineering, Korea Institute of Science and Technology (KIST),
5 Hwarang-ro 14-gil, Seongbuk-gu, Seoul 02792, Korea
(*Received 6 December 2017 • accepted 12 February 2018*)

Abstract−Kinetic models of CO hydrogenation to paraffinic hydrocarbons through Fischer-Tropsch synthesis (FTS) reaction were studied by using Langmuir-Hinshelwood Hougen-Watson (LHHW) model of 16 different reaction steps with a pseudo steady-state assumption (PSSA) on the prototype Pt-promoted Co/Al_2O_3 catalyst having a granule size of ~1 mm of spherical γ-Al_2O_3 support (surface area of 149 m^2/g). The derived kinetic models from ten sets of experimental data by altering the reaction conditions such as temperatures, pressures, space velocities and H_2/CO molar ratios were found to be well fitted with reasonable kinetic parameters and small errors of conversion of CO and hydrocarbon distributions in terms of mean absolute relative residual (MARR) and relative standard deviation error (RSDE). The derived reaction rates and CO activation energy of −86 kJ/mol well correspond to the our previously reported results using power-type catalysts. Based on the LHHW model with PSSA, the possible chemical intermediates on the granule ball-type Co-Pt/Al_2O_3 surfaces were precisely considered to explain the typical adsorption, initiation, propagation and termination steps of FTS reaction as well as to derive elementary reaction rates with their kinetic parameters and hydrocarbon distributions. The derived kinetic models were further used to verify temperature-profiles in a pilot-scale fixed-bed tubular FTS reactor with a packing depth of 100 cm catalyst, and it confirmed that the temperature gradients were less than 10 °C in a length of reactor by effectively removing the generated heat by an exothermic FTS reaction.

Keywords: Fischer-Tropsch Synthesis (FTS) Reaction, Cobalt-based FTS Catalyst, Kinetic Parameter Estimations, Langmuir-Hinshelwood Hougen-Watson (LHHW) Model, Pseudo Steady-state Assumption (PSSA)

INTRODUCTION

Fischer-Tropsch Synthesis (FTS) reaction, which is a typical CO hydrogenation reaction of hydrocarbons, is a crucial chemical unit for an alternative conversion technology of natural gas (or shale gas) to environmentally benign fuels and petrochemicals [1]. Since the FTS reaction is a key unit of the gas-to-liquids (GTL) process composed of three typical units such as reforming of hydrocarbons, FTS and hydrotreating reaction, reactor design and kinetic studies of FTS reaction as well as catalyst developments have been widely studied in many commercial scale reactors [1-4]. For example, two different operating conditions for FTS reaction have been commercially established, such as high-temperature Fischer-Tropsch (HTFT) and low-temperature Fischer-Tropsch (LTFT) reaction with different catalytic reactors [4]. The HTFT process has the characteristics of operating temperature of ~300 °C using iron-based FTS catalysts applied to SASOL plants for a selective light olefin production using a fixed or circulating fluidized-bed reactor. The LTFT process has been generally operated at ~220 °C with cobalt-based FTS catalysts for the preferential production of linear higher molecular-weight hydrocarbons using a gas-phase multi-tubular fixed-bed reactor or liquid-phase slurry bubble-column reactor operated by SHELL and SASOL plants [4]. Even though many process simulations with optimal FTS catalysts have been reviewed with specific reactor types, a relatively small endeavor has been made and reported in the fields of detailed descriptions of FTS reaction kinetics using the commercial-scale FTS catalysts till now as far as we know.

In terms of FTS catalyst development, many reports have focused on designing the active Al_2O_3 or SiO_2-supported cobalt-based catalysts for a commercial implementation, such as in SASOL and SHELL's commercial GTL plants [1]. Among the active cobalt or iron-based commercial FTS catalysts, the cobalt-based catalysts have been more intensively studied in order to obtain a higher catalytic activity and stability with selective productions of paraffinic heavy wax hydrocarbons, which can be acquired by designing the highly dispersed cobalt nanoparticles on the highly mesoporous supporting materials with some chemical promoters such as Pt and Ru metals [5,6]. Among the various deactivation mechanisms of cobalt-based FTS catalysts, the effective suppression methods of the supported active cobalt nanoparticles' aggregations have been successfully carried out using the structural promoters such as phos-

†To whom correspondence should be addressed.
E-mail: mjpark@ajou.ac.kr, finejw@skku.edu

phorous or transition metal oxides using porous supports having a larger pore size [1,7-9].

In the present investigation, the reaction kinetics for a fixed-bed tubular FTS reactor design using a commercial-scale spherical Pt-promoted Co/Al_2O_3 catalyst (Co-Pt/Al_2O_3) with 1 mm diameter and large mesopore size of 8.5 nm were developed based on the proposed reaction mechanisms from our previous studies [10-12]. The developments of kinetic models of a fixed-bed LTFT reactor were studied to design an efficient tubular FTS reactor as well as to develop a proper methodology of a fixed-bed reactor scale-up. The preliminary investigation for the fundamental properties of a prototype Co-Pt/Al_2O_3 catalyst was experimentally carried out and the kinetics models based on Langmuir-Hinshelwood Hougen-Watson (LHHW) models with the 16 different reaction steps proposed were further developed by using the spherical prototype Co-Pt/Al_2O_3 catalyst.

EXPERIMENTAL SECTIONS

1. Preparations of Spherical Co-Pt/Al_2O_3 Catalyst and Activity Measurements

The porous γ-Al_2O_3 as a supporting material of active metals having a diameter of 1 mm with a spherical ball (average mesopore size of 8.4 nm with surface area of 149 m^2/g) was previously calcined at 500 °C for 3 h to prevent any surface cracks or disintegrations of ball structures during the impregnation step of active metal precursors. The prototype Pt-promoted Co/Al_2O_3 catalyst (Co-Pt/Al_2O_3) was prepared by a typical wet impregnation method at a fixed weight of cobalt and platinum metals of 20 wt% and 0.1 wt% (metal-based on the support), respectively. Two different metal precursors such as cobalt(II) nitrate hexahydrate ($Co(NO_3)_2{\cdot}6H_2O$) and chloroplatinic acid hydrate ($H_2PtCl_6{\cdot}xH_2O$), which was used as a chemical promoter, were dissolved in deionized water solvent simultaneously, and the slurry of the precursor solutions with spherical γ-Al_2O_3 ball was further stirred in a vacuum rotary evaporator at 60 °C for 3 h, followed by drying the slurry at the same temperature under vacuum condition. The sample was subsequently dried in an oven maintained at 110 °C for ~12 h carefully and then as-prepared Co-Pt/Al_2O_3 catalyst was calcined with stepwise calcination steps such as at 350 °C for 1 h and at 450 °C for 3 h. The final FTS catalyst was denoted as CoPt/Al, where the Al represents the spherical γ-Al_2O_3 ball with a granule diameter of 1 mm and mesopore diameter of 8.5 nm.

FTS reaction was carried out with 0.5 g catalyst loading in a 3/8 inch tubular fixed-bed reactor with an inner diameter of 0.7 mm. Before carrying out FTS reaction, the CoPt/Al was activated at 400 °C for 12 h under a reductive gas flow of 5 vol%H_2 balanced with N_2 as a reducing agent at a flow rate of 25 ml/min. After the CoPt/Al activation, the tubular reactor was cooled to room temperature and the pressure was subsequently increased to the desired reaction pressure under a flow of reaction syngas mixtures of H_2/CO with an internal standard gas of 5.5 vol%N_2. For the kinetic experiments, the ten separate sets of FTS reaction were performed under various reaction conditions such as T=220-250 °C, P=10-20 bar, SV=2,000-4,000 h^{-1}, and H_2/CO molar ratio=1.5-2.5. All the kinetic experiments were separately carried out for 60 h, and the average values (for 20 h) just after approaching a steady-state CO conversion and product distribution after 40 h reaction were used to estimate the kinetic parameters. The effluent gases from the exit of the FTS reactor were simultaneously analyzed by using an on-line YoungLin gas chromatograph (YL Acme 6000 GC) installed with a Carboxen 1000 packed column connected to a thermal conductivity detector (TCD) as well as by using a GS-GASPRO capillary column equipped with a flame ionization detector (FID). For more details, the effluent gases of H_2, N_2, CO, CH_4 and CO_2 were in-situ analyzed by TCD and the formed hydrocarbons up to the carbon number of C_8 were analyzed by FID. In addition, the heavy wax hydrocarbons captured in a cold-trap kept at 60 °C at the end of reactor were analyzed by off-line GC for calculating liquid hydrocarbon distributions, which were analyzed by using an Agilent 7890A GC equipped with HP-PONA column connected to FID. The CO conversion and product distribution on the prototype CoPt/Al at various reaction conditions were calculated by using total carbon-balances with a total carbon error range below 2%.

2. Characterization of Co-Pt/Al_2O_3 Catalyst

The physical properties of specific surface area, average pore diameter and pore volume of the fresh CoPt/Al and pristine γ-Al_2O_3 support itself were characterized by using a Tristar II instrument (Micromeritics). Prior to N_2 adsorption-desorption analysis, the CoPt/Al was pretreated by a stepwise heat treatment under a vacuum condition such as at 90 °C for 1 h and at 350 °C for 4 h. The isotherms of N_2 adsorption-desorption were finally obtained at a liquid nitrogen temperature of –196 °C by maintaining the pressure of 10^{-6} Pa. The separate specific surface area and pore size distribution of the fresh CoPt/Al were determined by Brunauer-Emmett-Teller (BET) method and Barrett-Joyner-Halenda (BJH) method using the desorption isotherm. The characteristic diffraction patterns of the fresh CoPt/Al were obtained by using a powder X-ray diffraction (XRD) instrument (Bruker D8 ADVANCE) operating at 40 kV and 100 mA with a Cu-Kα radiation of λ=1.5406 Å at a scanning speed of 5 °C/min. The cluster size of spinel cobalt oxide (Co_3O_4) on the fresh CoPt/Al was determined by using the values of full width at half maximum (FWHM) with the largest diffraction peak of the Co_3O_4 located at 2θ=36.8° with the help of Debye-Scherrer equation. The crystallite size of metallic cobalt (Co^0) was further calculated by the equation of volume contraction correlation of $d(Co^0)=0.75 \times d(Co_3O_4)$, which takes into account the relative molar volume change of the spinel Co_3O_4 and metallic cobalt species.

H_2-temperature programmed reduction (TPR) analysis was also performed to confirm the reducibility of the supported cobalt nanoparticles on the fresh CoPt/Al. The CoPt/Al with 30 mg sample was loaded into a BELCAT-M instrument installed with a TCD and the sample was pretreated at 250 °C for 1 h at a helium flow rate of 30 ml/min. After subsequent cooling to 50 °C, 10%H_2/Ar flowed at a helium flow rate of 30 ml/min to stabilize TCD signal at the same temperature. Finally, TPR patterns were obtained by increasing the temperature to 700 °C at a ramping speed of 10 °C/min. The water generated during TPR experiment was simultaneously removed in a cold trap filled with molecular sieve (5A). Transmission electron microscopy (TEM) analysis was also performed by a JEM ARM 200F instrument to verify the changes of surface

morphologies of alumina and crystallite sizes of the cobalt nanoparticles on the fresh and used CoPt/Al, and their surface images were further verified by a field emission scanning electron microscope (Mira II LMH, FE-SEM) to verify the changes of outer surface morphologies of the spherical γ-Al_2O_3 support during FTS reaction.

RESULTS AND DISCUSSION

1. Bulk and Surface Characteristics of Fresh Co-Pt/Al_2O_3 Catalyst

Specific surface areas (Sg, m^2/g), pore volumes (Pv, cm^3/g), average pore diameters (Pd, nm) and pore size distributions of the fresh CoPt/Al and spherical γ-Al_2O_3 ball itself are displayed in Fig. 1(a) and 1(b). The CoPt/Al and γ-Al_2O_3 showed a typical type IV hysteresis loop (supplementary Fig. S1), and they exhibited uniform and sharp pore size distributions at around 8 nm in size. The specific surface areas and pore volumes of the CoPt/Al were found to be a little smaller than those of the γ-Al_2O_3 itself from 149 to 127 m^2/g and 0.46 to 0.32 cm^3/g with similar average pore diameters of 8.4-8.5 nm, respectively. These slightly decreased values on the CoPt/Al appear to be attributed to the selective and uniform depositions of cobalt and platinum nanoparticles on the outer mesopores of spherical γ-Al_2O_3 surfaces. This observation also revealed that those cobalt and platinum nanoparticles were preferentially distributed on the outer surfaces rather than the inside of γ-Al_2O_3 support by forming a core-shell type heterogeneous CoPt/Al catalyst. The XRD patterns of the fresh CoPt/Al are shown in Fig. 1(c), and the characteristic surface planes of spinel-type Co_3O_4 such as (111), (220), (311), (222), (400), (422), (511), (440), (531) and (533) were clearly observed at diffraction peak positions of 18.9, 31.3, 36.9, 38.6, 45.0, 55.8, 59.5, 65.4, 67.1 and 77.3°, respectively [13-15]. The calculated crystallite size of the Co_3O_4 using the most intense Co_3O_4 diffraction peak located at 2θ=36.9° was ~17.7 nm, which was larger than that of the mesopores of pristine γ-Al_2O_3 support, strongly suggesting the preferential outer surface distributions of cobalt nanoparticles as verified by N_2 sorption analysis.

The reduction behavior of the fresh CoPt/Al was analyzed by TPR analysis, and the TPR peaks are displayed in Fig. 1(d). The well-reported two-step successive reductions of the supported Co_3O_4 nanoparticles [16-19] were clearly observed on the CoPt/Al through the reduction of Co_3O_4 to CoO and its successive reduction to metallic cobalt at ~300 °C and above 350 °C, respectively [20]. Interestingly, the observed first reduction peak below 300 °C was signifi-

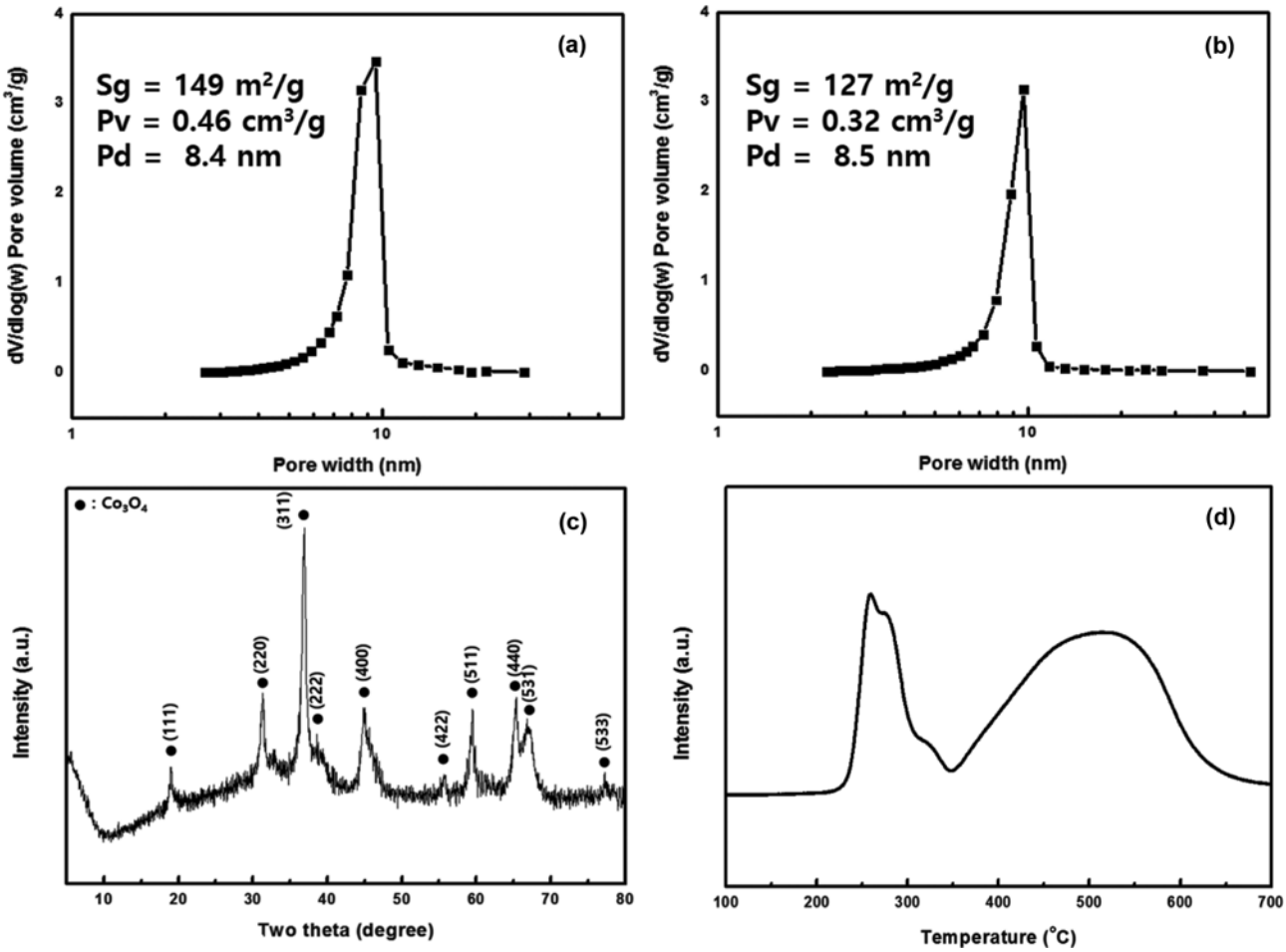

Fig. 1. Pore size distributions of (a) spherical γ-Al_2O_3 itself (granule size of 1 mm), (b) fresh Co-Pt/Al_2O_3 catalyst by N_2 adsorption-desorption analysis, (c) XRD patterns of the fresh Co-Pt/Al_2O_3 catalyst, and (d) TPR profiles of the fresh Co-Pt/Al_2O_3 catalyst.

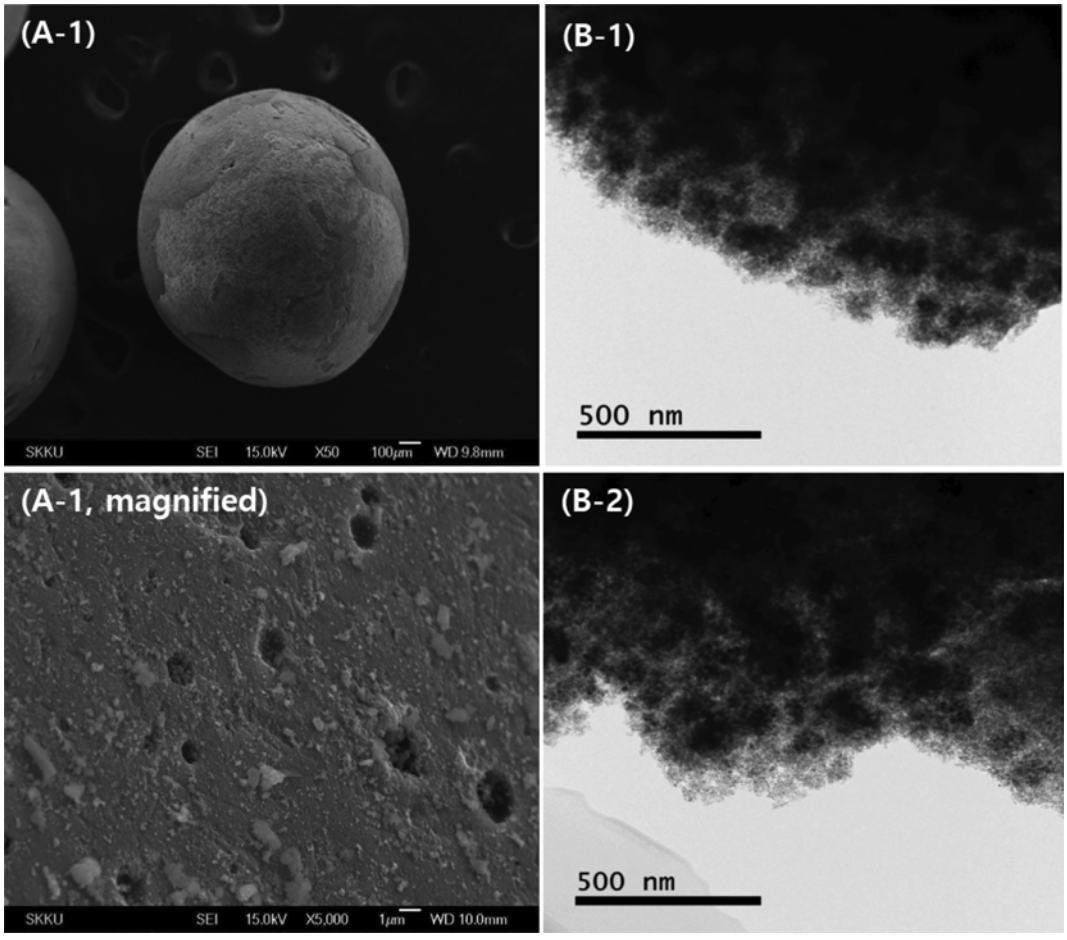

Fig. 2. (A) SEM and (B) TEM images of the (1) fresh and (2) used Co-Pt/Al_2O_3 catalyst.

cantly lower than some conventional cobalt-based FTS catalysts [7-12,14,20], which can be possibly attributed to a facile hydrogen spillover by platinum promoter and its preferential depositions on the most outer surfaces of the γ-Al_2O_3 support. The broad reduction peak at 350-700 °C also indicated the much stronger metal-support interactions between small cobalt nanoparticles and acidic surfaces of γ-Al_2O_3. The SEM and TEM images of the fresh and used CoPt/Al are displayed in Fig. 2, and the morphology of the spherical γ-Al_2O_3 and cobalt nanoparticles were insignificantly altered even after FTS reaction at 230 °C for reaction duration of 60 h. The distribution of the cobalt nanoparticles on the outer surfaces of the γ-Al_2O_3 was confirmed by TEM images with an average cobalt particle size of ~20 nm as shown in Fig. 2(B), and no significant heavy wax depositions were observed on the outer surfaces of the used CoPt/Al, which seems to be possibly responsible for an insignificant catalyst deactivation of the spherical prototype CoPt/Al (diameter of 1 mm) under all the kinetic experiment conditions as well.

2. Reaction Mechanisms and Rate Equations for FTS Reaction

Kinetic studies, including the derivations of kinetic parameters and rate equations on the spherical ball-type CoPt/Al, were carried out based on the 16 different LHHW mechanisms and kinetic models presented in our previous studies [10-12]. The FTS reaction mechanisms used in the present investigation are summarized in Table 1 with the elementary reaction steps and their rate equations for the separate adsorptions of CO, H_2 and H_2O, initiation, propagation and termination steps of chemical intermediates formed. The selective formations of methane, paraffinic and olefinic hydrocarbons were also considered to derive proper kinetic parameters on the CoPt/Al. For example, the adsorbed intermediates of Rn*, representing alkylidene (C_nH_{2n+1}), as well as P_n and O_n for the respective paraffin (C_nH_{2n+2}) and olefin (C_nH_{2n}) products are summarized in Table 1 with the appendix for kinetic symbols of chemical intermediates and reaction variables. All elementary reaction steps were proposed based on the previous results from various literatures [1,3,21-31]. For more details, the adsorption step of hydrogen was assumed to be a dissociative reversible adsorption step [21-23], and that of CO molecule was assumed to be reversible and its dissociation step was considered as irreversible elementary reaction and so on [1] with a simultaneous reversible adsorption of water formed as well. In addition, the formation steps of final products such as methane and paraffinic hydrocarbons were considered as irreversible reactions, and that of olefinic hydrocarbons was assumed as a reversible reaction due to its well-known secondary reaction activities to form much higher molecular-weight hydrocarbons [1,3]. Furthermore, the reaction rates based on the respective elementary steps are also summarized in Table 1, and the formation rates of the main FTS products of methane, paraffinic and olefinic hydrocarbons were derived with the following two assump-

Table 1. Proposed reaction mechanisms on the Co-based FTS catalysts

No.	Mechanism		Remarks	Reference
1	$H_2+2^* \rightleftharpoons 2H^*$	$K_{H_2}^{ad}=\frac{\theta_{H_*}^2}{P_{H_2}\theta_*^2}$	Adsorption	[21-23]
2	$CO+* \rightleftharpoons CO^*$	$K_{CO}^{ad}=\frac{\theta_{CO^*}}{P_{CO}\theta_*}$		[21]
3	$H_2O+* \rightleftharpoons H_2O^*$	$K_{H_2O}^{ad}=\frac{\theta_{H_2O^*}}{P_{H_2O}\theta_*}$		
4	$O_n+* \rightleftharpoons O_n^*$	$K_{O_n}^{ad}=\frac{\theta_{O_n*}}{P_{O_n}\theta_*}$ $n\geq 2$		
5	$CO^*+* \xrightarrow{k_{CO}} C^*+O^*$	$r_{CO}=k_{CO}\theta_{CO^*}\theta_*$		[1]
6	$C^*+H^* \xrightarrow{k_C} CH^*+*$	$r_C=k_C\theta_{C^*}\theta_{H^*}$		[24,25]
7	$CH^*+H^* \xrightarrow{k_{CH}} CH_2^*+*$	$r_{CH}=k_{CH}\theta_{CH^*}\theta_{H^*}$		[24,25]
8	$O^*+H^* \xrightarrow{k_{OH}} OH^*+*$	$r_{OH}=k_{OH}\theta_{O^*}\theta_{H^*}$		[26-28]
9	$OH^*+H^* \xrightarrow{k_W} H_2O^*+*$	$r_W=k_W\theta_{OH^*}\theta_{H^*}$		[26-28]
10	$CH_2^*+H^* \xrightarrow{k_{IN}} CH_3^*+*$	$r_{IN}=k_{IN}\theta_{CH_2^*}\theta_{H^*}$	Initiation	[29]
11	$R_n^*+CH_2^* \xrightarrow{k_G} R_{n+1}^*+*$	$r_{G,n}=k_G\theta_{R_n^*}\theta_{CH_2^*}$ $n\geq 1$	Propagation	[30]
12	$CH_3^*+H^* \xrightarrow{k_{CH_4}} CH_4+2^*$	$r_{CH_4}=k_{CH_4}\theta_{CH_3^*}\theta_{H^*}$	Termination	[26,27]
13	$R_2^*+H^* \xrightarrow{k_{P_2}} P_2+2^*$	$r_{P,2}=k_{P_2}\theta_{R_2^*}\theta_{H^*}$		[26,27]
14	$R_n^*+H^* \xrightarrow{k_{P_n}} P_n+2^*$	$r_{P,n}=k_{P_n}\theta_{R_n^*}\theta_{H^*}$ $n\geq 3$		[26,27]
15	$R_2^*+* \underset{k_{O_2}^{rev}}{\overset{k_{O_2}}{\rightleftharpoons}} O_2^*+H^*$	$r_{O,2}=k_{O_2}\theta_{R_2^*}\theta_*-k_{O_2}^{rev}\theta_{O_2^*}\theta_{H^*}$		[3,32]
16	$R_n^*+* \underset{k_{O_n}^{rev}}{\overset{k_{O_n}}{\rightleftharpoons}} O_n^*+H^*$	$r_{O,n}=k_{O_n}\theta_{R_n^*}\theta_*-k_{O_n}^{rev}\theta_{O_n^*}\theta_{H^*}$ $n\geq 3$		[3,32]

Table 2. Catalytic activity and product distributions at various reaction conditions on the Co-Pt/Al_2O_3 catalyst

Case #	Temperature (°C)	Pressure (bar)	SV (h^{-1})	H_2/CO ratio	CO conversion	Product distributions (mol%)[a]										
						CO_2	C_1	C_2	C_3	C_4	C_5	C_6	C_7	C_8	C_9+	α
1	220	20	3000	2	69.19	0.24	16.04	1.28	1.60	1.23	0.97	0.56	0.25	0.15	77.92	0.934
2	230	20	3000	2	83.04	0.79	16.39	1.31	1.63	1.20	0.89	0.47	0.18	0.09	77.84	0.905
3	240	20	3000	2	86.06	1.27	19.77	1.66	2.03	1.45	1.04	0.55	0.21	0.11	73.18	0.905
4	250	20	3000	2	87.83	2.04	22.72	2.01	2.32	1.60	1.19	0.64	0.24	0.13	69.15	0.903
5	230	15	3000	2	70.11	0.46	18.16	1.50	1.86	1.44	1.16	0.71	0.30	0.19	74.68	0.923
6	230	25	3000	2	82.67	0.82	11.77	0.95	1.43	1.07	0.77	0.41	0.17	0.09	83.34	0.930
7	230	20	2000	2	87.13	1.26	12.21	0.86	1.42	1.06	0.78	0.42	0.16	0.09	83.00	0.900
8	230	20	4000	2	69.12	0.42	18.36	1.51	1.82	1.36	1.08	0.66	0.29	0.19	74.73	0.900
9	230	20	3000	1.5	53.86	0.37	8.99	0.78	1.24	1.03	0.82	0.50	0.26	0.18	86.18	0.933
10	230	20	3000	2.5	92.43	0.50	24.80	1.83	2.01	1.32	0.96	0.47	0.18	0.10	68.33	0.935

[a]Product distributions of each carbon number up to C_8 with carbon dioxide were calculated by total carbon balances using the steady-state values with the average values for 20 h reaction duration after 40 h on stream, and chain-growth probability of alpha value (α) was calculated using Anderson-Schulz-Flory (ASF) equation in the ranges of C_9-C_{30} hydrocarbons

tions.

(1) Pseudo-steady state assumption (PSSA) was applied for the formation of chemical intermediates that 0^{th} moment to obtain the total amount of living chain species.

(2) Specificity for a formation of methane is not so significant.

All proposed reaction rates based on the LHHW models with ten different experimental sets as summarized in Table 2 are listed below, and they were further applied to estimate kinetic parameters and activation energy on the CoPt/Al (Table 3 and Table 4), which are more accurately explained in the following section, 3.4.

$$r_{CH_4}=k_{CH_4}\alpha_1\alpha_H/\mathrm{DEN}$$

Table 3. Summarized results from ten experimental cases to derive the kinetic parameters

	Case 1	Case 2	Case 3	Case 4	Case 5	Case 6	Case 7	Case 8	Case 9	Case 10
CO conv. [%]	69.19	83.04	86.06	87.83	70.11	82.67	87.13	69.12	53.86	92.43
CH_4 sel. [%]	16.04	16.39	19.77	22.72	18.16	11.77	12.21	18.36	8.99	24.80
paraffin sel. [%]	1.24	1.28	1.63	1.98	1.46	0.91	0.84	1.47	0.70	1.82
olefin sel. [%]	0.04	0.03	0.03	0.03	0.04	0.04	0.02	0.04	0.08	0.01
No(avg) HC[a]	13.11	11.55	10.78	10.51	12.53	14.11	12.23	11.46	14.31	11.56
Wt(avg) HC[b]	18.60	15.89	15.31	16.09	17.76	18.88	16.39	16.64	18.47	18.41
No(avg) paraffin (P2)[c]	18.42	16.30	15.63	15.04	16.70	18.46	16.95	16.74	18.73	17.81
Wt(avg) paraffin (P2)[d]	21.34	18.81	18.31	18.35	19.30	21.32	19.68	19.97	21.01	21.43
No(avg) olefin (O2)[e]	19.61	17.83	17.16	19.76	19.28	18.88	18.51	17.76	18.58	20.82
Wt(avg) olefin (O2)[f]	22.82	20.41	19.37	23.22	22.30	21.95	21.45	21.01	21.49	23.84

[a]No(avg) HC represent the average carbon numbers of hydrocarbons formed
[b]Wt(avg) HC represents the average molecular weights of hydrocarbons formed
[c]No(avg) paraffin (P2) represents the average carbon numbers (above C_2) of paraffinic hydrocarbons formed
[d]Wt(avg) paraffin (P2) represents the average molecular weights (above C_2) of paraffinic hydrocarbons formed
[e]No(avg) olefin (O2) represents the average carbon numbers (above C_2) of olefinic hydrocarbons formed
[f]Wt(avg) olefin (O2) represents the average molecular weights (above C_2) of olefinic hydrocarbons formed

Table 4. Estimated kinetic parameters in this study

Parameter	Value	Unit
Kinetic parameters at reference temperature of 230 °C		
$K_{H_2}^{ad}$	4.67 E-04	bar^{-1}
$k_{CO}K_{CO}^{ad}$	7.95 E-01	mol/kg/s/bar
k_{IN}	2.10 E-01	mol/kg/s
k_G	1.35 E+00	mol/kg/s
k_{CH_4}	4.60 E+01	mol/kg/s
k_{P_n}	1.43 E+01	mol/kg/s
k_{P_2}	3.75 E+00	mol/kg/s
k_{O_n}	2.08 E-01	mol/kg/s
$k_{O_n}^{rev}K_{O_n}^{ad}$	1.96 E+00	mol/kg/s/bar
k_{O_2}	1.26 E-02	mol/kg/s
$k_{O_2}^{rev}K_{O_2}^{ad}$	5.33 E+00	mol/kg/s/bar
Activation energy		Ref [12]
$(E+\Delta H)_{CO}$	−86.516 kJ/mol	−159.8 kJ/mol
E_G	5.030 kJ/mol	
E_{P_n}	9.903 kJ/mol	

$$r_{P,2}=k_{P_2}(A_2\alpha_1+B_2)\alpha_H/DEN$$

$$r_{P,n}=k_{P_n}\left\{A^{n-2}A_2\alpha_1+\left(\sum_{i=2}^{n}A^{n-1}B_i\right)\right\}\alpha_H/DEN,\ n\geq 3$$

$$r_{O,2}=\{k_{O_2}(A_2\alpha_1+B_2)-k_{O_2}^{rev}K_{O_n}\alpha_H P_{O_2}\}/DEN$$

$$r_{O,n}=\left[k_{O_n}\left\{A^{n-2}A_2\alpha_1+\left(\sum_{i=2}^{NP}A^{n-i}B_i\right)\right\}-k_{O_n}^{rev}K_{O_n}\alpha_H P_{O_n}\right]/DEN,\ n\geq 3$$

where, $DEN=[1+\alpha_H+\alpha_{CH_2}+\{(1+\Sigma_{k=2}^{NP}A^{k-2}A_2)\alpha_1+(\Sigma_{k=2}^{NP}\Sigma_{i=2}^{k}A^{k-i}B_i)\}]^2$

$$A_2=\frac{k_G\alpha_{CH_2}}{k_G\alpha_{CH_2}+k_{P_2}\alpha_H+k_{O_2}}\quad A_n=\frac{k_G\alpha_{CH_2}}{k_G\alpha_{CH_2}+k_{P_n}\alpha_H+k_{O_n}}$$

$$B_2=\frac{k_{O_2}^{rev}K_{O_n}\alpha_H P_{O_2}}{k_G\alpha_{CH_2}+k_{P_2}\alpha_H+k_{O_2}}\quad B_n=\frac{k_{O_n}^{rev}K_{O_n}\alpha_H P_{O_n}}{k_G\alpha_{CH_2}+k_{P_n}\alpha_H+k_{O_n}}$$

$$\alpha_1=\frac{k_{IN}\alpha_{CH_2}\alpha_H}{k_G\alpha_{CH_2}+k_{CH_4}\alpha_H}\quad \alpha_H=(K_{H_2}^{ad}P_{H_2})^{1/2}\quad \alpha_{CH_2}=\frac{-\beta_2+\sqrt{\beta_2^2+4\beta_1\beta_3}}{2\beta_1}$$

$$\beta_1=\frac{k_G k_{IN}}{k_{P_n}+k_{O_n}\alpha_H^{-1}}\quad \beta_2=k_{IN}\alpha_H+\frac{k_G k_{O_n}^{rev}K_{O_n}(\Sigma_{n=2}^{\infty}P_{O_n})}{k_{P_n}+k_{O_n}\alpha_H^{-1}}\quad \beta_3=k_{CO}K_{CO}P_{CO}$$

where, r, k_j, and K_i^{ad} represent reaction rates in the unit of mol/kg/s, where rate constants of the elementary reaction of j and equilibrium constant of species i, respectively.

3. Effects of Reaction Variables to Catalytic Performances on Co-Pt/Al_2O_3 Catalyst

The effects of reaction variables to catalytic performances such as temperature (°C), pressure (bar), space velocity (SV, h^{-1}) and H_2/Co molar ratio on the CoPt/Al are summarized in Table 2. To further estimate the kinetic parameters and activation energy, the separate ten different experimental sets were performed, and two different GCs were applied to calculate the CO conversion and product distributions displayed with two significant digits, where C_9+ hydrocarbons were analyzed by using an off-line GC by using the corrected liquid samples formed. As shown in Fig. 3, the catalytic stability of the CoPt/Al at all reaction conditions was relatively stable for 60 h on stream with larger activity changes according to the reaction variables, especially with feed molar ratios of H_2/CO. A little bit significant decreases of CO conversions at higher SVs above 4,000 h^{-1} and lower pressure below 15 bar at steady-state as shown in Fig. 3(b) and 3(c) seem to be attributed to the structural reconstructions of cobalt nanoparticles by the facile depositions of heavy hydrocarbons, which may cause an increased CH_4 selectivity [3,14,20]. The product distributions and value of chain-growth probability (α) calculated by a polymerization mechanism with Anderson-Schulz-Flory (ASF) equation are also summarized in Table 2 and supplementary Fig. S2, which clearly revealed the effects of reaction variables. As shown in Fig. 4, higher CO conversions and

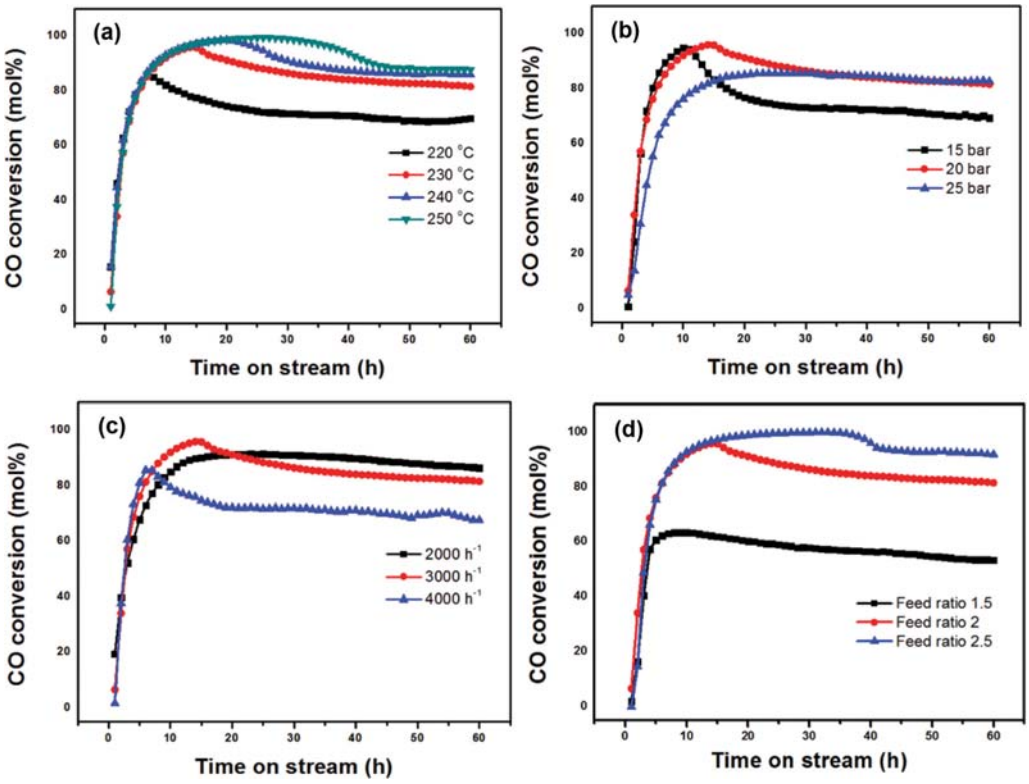

Fig. 3. Catalytic activity on the Co-Pt/Al_2O_3 catalyst with time on stream (h) at the reaction variables of (a) reaction temperatures, (b) reaction pressures, (c) space velocities (SV), and (d) feed molar ratios of H_2/CO.

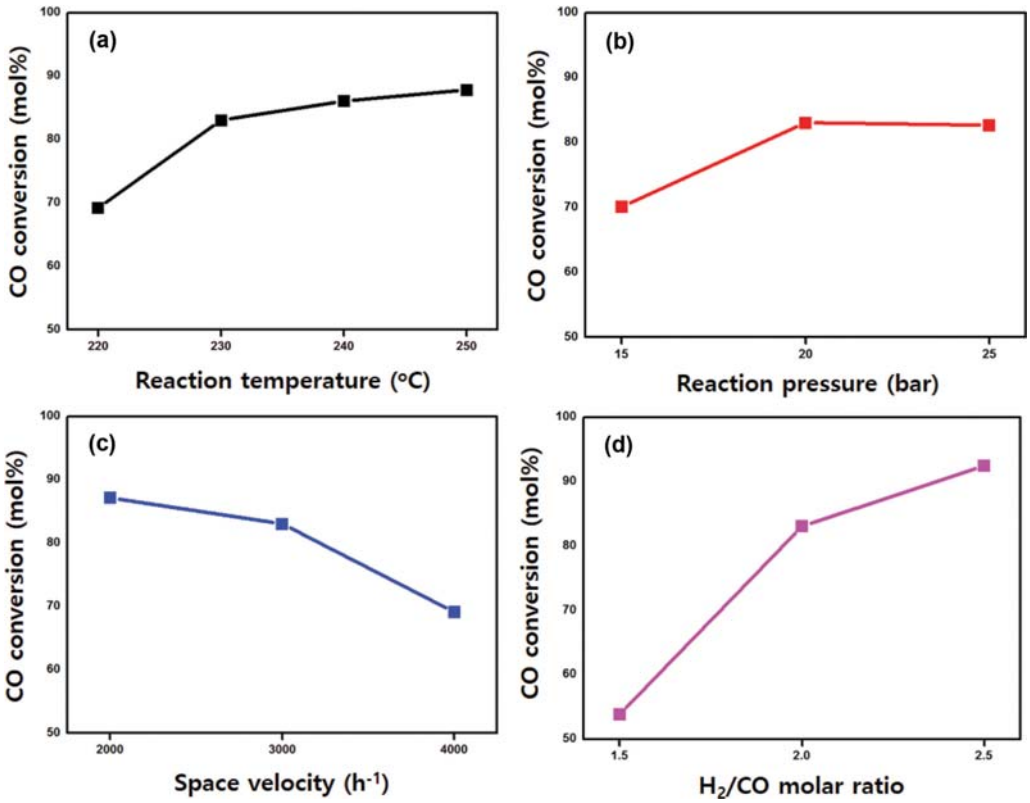

Fig. 4. Effects of reaction variables to CO conversion on the CoPt/Al; (a) reaction temperatures, (b) reaction pressures, (c) space velocities (SV), and (d) feed molar ratios of H_2/CO.

lower heavy hydrocarbon formations above C_{5+} were typically observed at a higher reaction temperature, lower pressure, higher SV and lower H_2/CO molar ratio, which are in line with the general phenomena of FTS reaction on the cobalt-based catalysts [1]. For example, if the reaction temperatures were increased from 220 to 250 °C, CO conversions were increased from ~69% to ~88% with the increased methane selectivity from ~16 to ~23% and vice versa in C_{5+} selectivity due to its higher initiation rate constants than the growth reaction rate constants [12]. Similarly, the effects of H_2/CO molar ratios on CO conversions were more significant and the undesired methane formation of ~25% was largely increased while increasing the feed H_2/CO molar ratio above 2.5 due to facile full hydrogenation activity of the intermediates to light hydrocarbons. Interestingly, CO conversion tended to increase slightly as the pressure increased above 20 bar, and the selectivity to methane was largely decreased while increasing the reaction pressures due to the increased amounts of adsorbed reactants to selectively form heavy hydrocarbons on the CoPt/Al. The changes of SVs revealed the greatest effects on CO conversions compared to other variables due to the largely changed residence times in the catalyst-bed, which were also observed in the experimental sets of 2, 7 and 8 in Table 2 with constant average molecular weight distributions. This observation suggests that the changes of SVs can be an easier and useful way to increase the productivity of heavy wax hydrocarbons on the highly active nano-sized cobalt-based catalysts with their less aggregation and less wax depositions [14].

4. Estimations of Kinetic Parameters on Co-Pt/Al_2O_3 Catalyst

Based on the kinetic models with experimental data on the spherical ball-type CoPt/Al, CO conversion, selectivity and average chain lengths of hydrocarbons on all the experimental cases are summarized in Table 3. From those experimental data, the maximum chain lengths of the formed hydrocarbons were analyzed up to C_{35}, and the chain lengths of C_2 to C_4 and C_{13} to C_{35} were further applied to calculate the average hydrocarbon chain lengths as summarized in Table 3 for deriving the kinetic parameters using the proposed 16 steps of LHHW reaction mechanisms in Table 1. The calculation formula of number average hydrocarbons (HC) and weight average HC are briefly summarized below.

$$\text{no.avg.HC} = \frac{\Sigma(\text{carbonnumber} \times \text{HC mol\%})}{\Sigma\text{HC mol\%}}$$

$$\text{wt.avg.HC} = \frac{\Sigma(\text{carbonnumber}^2 \times \text{HC mol\%})}{\Sigma(\text{no.avg.HC} \times \text{HC mol\%})}$$

In addition, the fractions of paraffinic and olefinic hydrocarbons

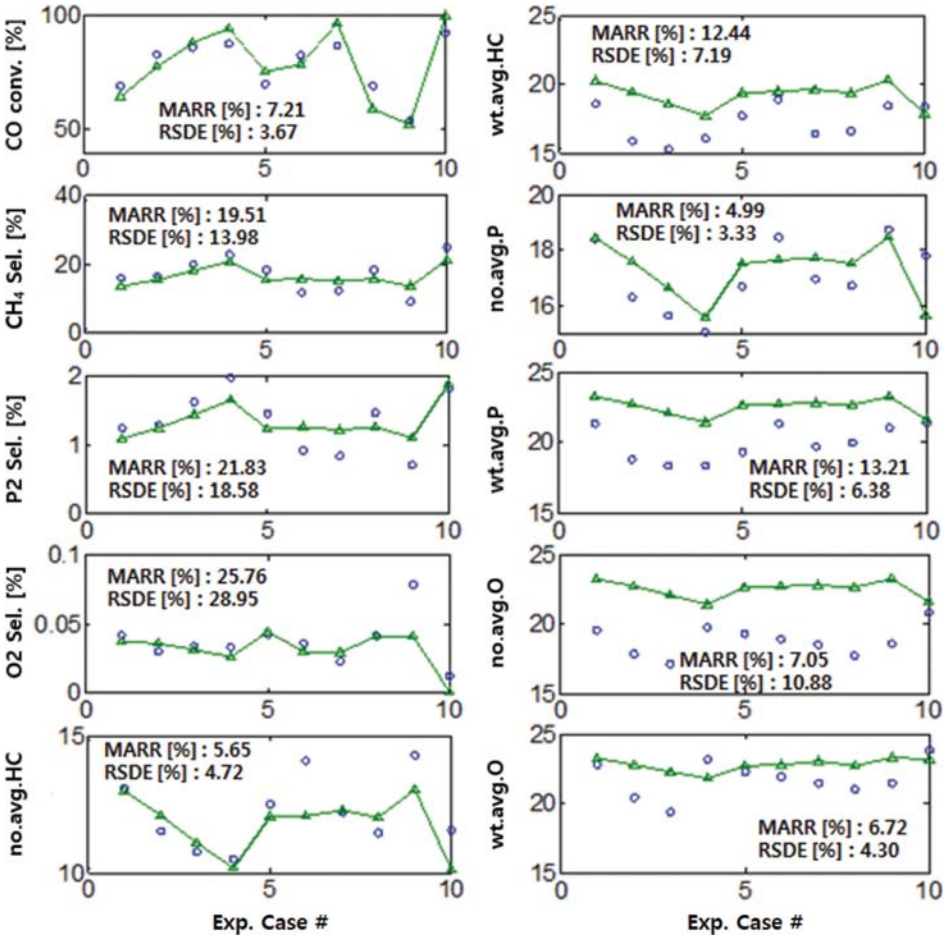

Fig. 5. Fitting results between experimental data (blue blank circle) and simulated data (green blank triangle with solid line) from the proposed kinetic equations using carbon numbers below C_{35} (MARR [%] for mean absolute relative residual and rsde [%] for relative standard deviation error).

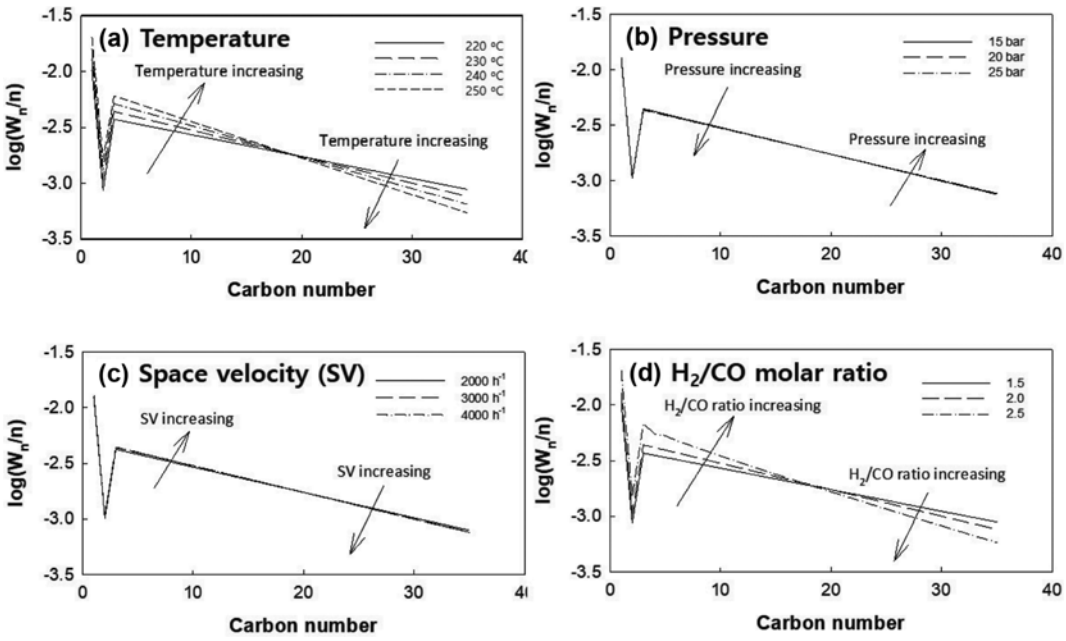

Fig. 6. Estimated hydrocarbon distribution fitted by Anderson-Schulz-Flory (ASF) distributions using the proposed reaction kinetics; (a) reaction temperatures of 220-250 °C, (b) reaction pressures of 15-25 bar, (c) space velocities (SV) of 2,000-4,000 h^{-1}, and (d) feed molar ratios of H_2/CO=1.5-2.5.

in C_2-C_4 and C_{13}-C_{35} were calculated using the Paraffin/Olefin ratio for all cases using the following equations as well.

$$\text{Paraffin fraction} = \frac{1}{1+\frac{1}{\text{P/O ratio}}}$$

$$\text{Olefin fraction} = \frac{1}{\text{P/O ratio}+1}$$

The calculated average carbon numbers (above C_2) of the paraffinic or olefinic hydrocarbons formed (denoted as P2 or O2) and average molecular weights (above C_2) of the paraffinic and olefinic hydrocarbons are also summarized in Table 3. By comparing the experimental data in Table 2 and simplified average values in Table 3, the fitting results of experimental data (blue blank circle) with the simulation results using the proposed reaction kinetics (green blank triangle and line) with the help of MATLAB program are summarized in Fig. 5. The fitted results between experimental and simulated data by using the kinetic equations with carbon numbers below 35 showed reasonable and acceptable errors such as mean absolute relative residual (MARR, %) and relative standard deviation error (RSDE, %) below ~20%. Well-fitted results of CO conversion and average carbon numbers with average molecular weights of paraffinic and olefinic hydrocarbons were obtained with less 10% errors of the v MARR and RSDE values. However, relatively larger errors of the selectivity of hydrocarbons such as methane and olefins were observed due to the presence of outlier points at a higher pressure and lower H_2/CO molar ratio (cases 6 and 9). This observation seems to be possibly attributed to the experimental errors at far from the normal operating conditions. However, since the final fitting results with the estimated kinetic equations seem to be reasonable to describe the experimental results, the parameter estimations and derivation of activation energy were further carried out and the results are summarized in Table 4. The derived rate constants and kinetic parameters with activation energies on the spherical CoPt/Al (1 mm ball-type) were well matched with the previous results, which was derived by using the powder-type cobalt-based catalysts [12,32]. From the estimated activation energy, it was confirmed that the CO adsorption and desorption steps have larger influences on the temperature dependent FTS reaction kinetics. Therefore, the initiation steps seem to be more sensitive to reaction variables than the chain growth or termination steps, which is consistent with the general ASF polymerization mechanisms as well. Finally, the ASF distribution under all the operating conditions were estimated using the proposed rate equations with the estimated kinetic parameters. The estimated ASF distributions from kinetic models as shown in Fig. 6 well correspond to experimental results as shown in supplementary Fig. S2, which confirms that the proposed reaction kinetics can properly estimate CO conversion with temperature profile in length and product distribution in a fixed-bed tubular FTS reactor. The hydrocarbon distribution from FTS reaction was significantly affected by the changes of temperatures and molar ratios of H_2/CO compared with those of space velocity and pressure. The heavy hydrocarbon formations were also decreased with an increase of temperature and H_2/CO molar ratio by the well-known FTS reaction mechanism by significantly suppressing secondary reactions of olefins formed [1-3]. In addition, reactor modeling using the derived kinetic equations was further carried out with mass and energy balance equations with proper boundary conditions as precisely described in our previous work [33]. As shown in Fig. 7, the temperature gradient in a spherical CoPt/Al catalyst-bed with its loading of 500 g and the packing depth of 100 cm in a tubular fixed-bed reactor with one-

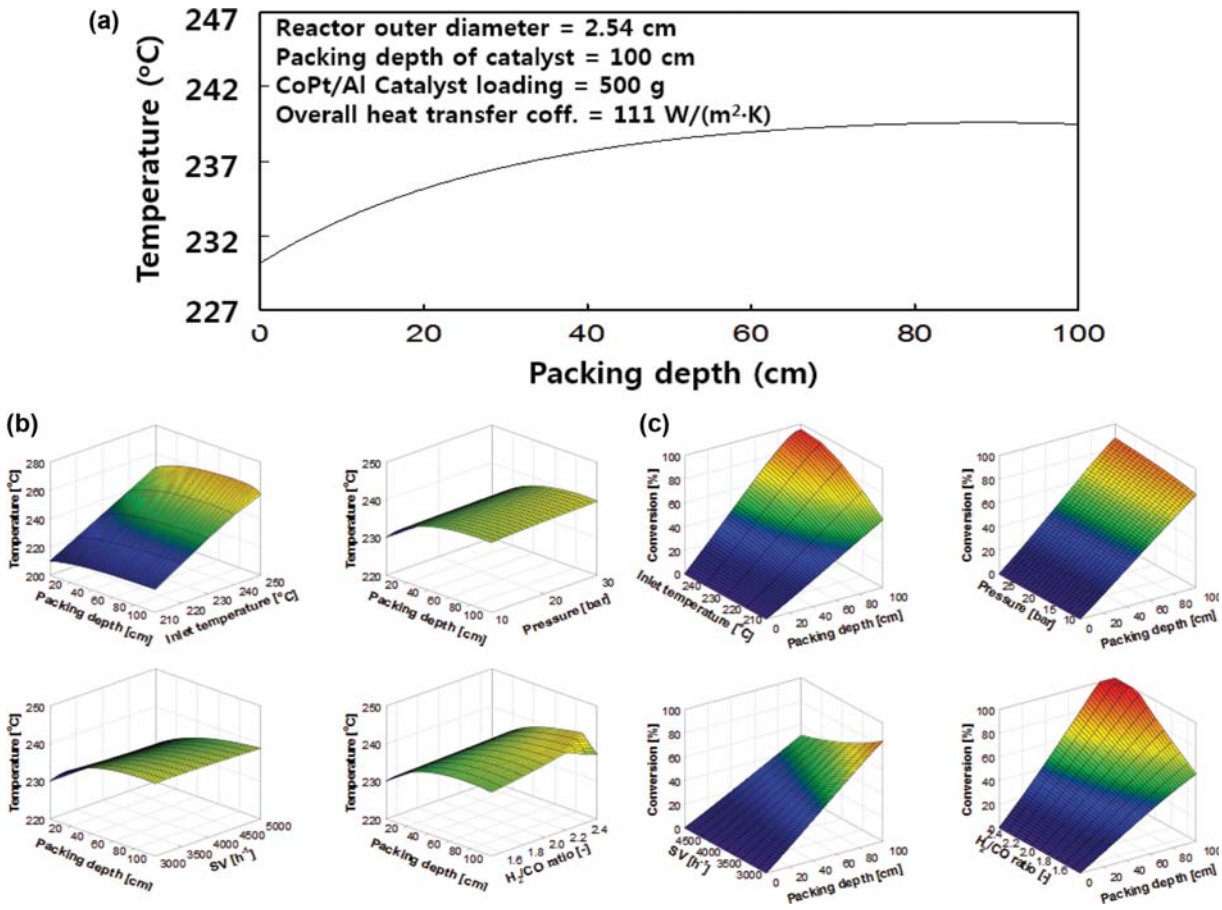

Fig. 7. Estimated temperature and CO conversion profiles in the spherical ball-type Co-Pt/Al_2O_3 catalyst (1 mm of diameter) with its packing depth of 100 cm according to reaction variables; (a) temperature profile with packing depth, (b) temperature profiles with respect to reaction variables and (c) CO conversion profiles with respect to reaction variables such as temperature, pressure, space velocity and H_2/CO molar ratio.

inch outer diameter was found to be less than 10 °C on all reaction variables such as inlet temperatures, pressures, SVs and H_2/CO molar ratios with an assumption of overall heat transfer coefficient of 100 W/(m^2·K) (Fig. 7(a)). According to the reaction variables such as inlet temperatures, pressures, SVs and H_2/CO molar ratios, the profiles of temperatures and CO conversions in the fixed-bed reactor are further displayed in Fig. 7(b) and 7(c), which clearly show the effects of reaction variables to the variations of CO conversion through the length of the fixed-bed reactor with a small temperature gradient. We believe that an even temperature profile in the catalyst-bed without significant hot-spot formation even under highly exothermic FTS reaction conditions can be attributed to the spherical ball-type shape (1 mm) of Co-Pt/Al_2O_3 catalyst by effectively removing the heat generated in the catalyst-bed.

In summary, the derived reaction kinetics and their parameters based on the LHHW models on the spherical ball-type Co-Pt/Al_2O_3 catalyst with the granule ball size of 1 mm were well fitted with the experimental data with reasonable errors, and the proposed rate equations can successfully estimate the CO conversion and product distributions. The derived kinetic models were further applied to effectively design a pilot-scale fixed-bed tubular FTS reactor using the spherical ball-type catalyst, and the temperature profiles with a catalyst packing depth of 100 cm revealed the temperature gradient of less than 10 °C by efficiently removing heat generated by the exothermic FTS reaction.

CONCLUSIONS

A prototype spherical Co-Pt/Al_2O_3 catalyst having a spherical ball-shape γ-Al_2O_3 with a ball-type granule size of 1 mm was applied to derive the reaction rate equations with their kinetic parameters of FTS reaction based on Langmuir-Hinshelwood Hougen-Watson (LHHW) mechanisms, which were composed of 16 separate steps of reaction mechanisms. The highly distributed cobalt nanoparticles on the outer surfaces of spherical γ-Al_2O_3 support showed a remarkably stable activity for 60 h on stream on all the ten tested sets of different reaction conditions like reaction temperatures of 220-250 °C, pressures of 15-25 bar, space velocities of 2,000-4,000 h^{-1} and feed H_2/CO molar ratios of 1.5-2.5. The derived kinetic models on the Pt-Co/Al_2O_3 also well described the experimental reaction results with reasonable errors of mean absolute relative residual (MARR) and relative standard deviation error (RSDE) below 20%. The derived reaction kinetics and their parameters can also successfully estimate the CO conversion and product distribu-

tions of heavy wax hydrocarbons below the carbon number of C_{35} through Anderson-Schulz-Flory (ASF) equation as well. The proposed kinetic models were also applied to design a fixed-bed tubular FTS reactor using the heterogeneous Pt-Co/Al_2O_3 catalyst without significant temperature gradients below 10 °C in the 100 cm of catalyst packing depth.

ACKNOWLEDGEMENTS

The authors sincerely acknowledge the financial support from the National Research Foundation (NRF) grant funded by the Korea government (NRF-2017R1D1A1B03028214).

LIST OF SYMBOLS

c : concentration [mol/L]
C_P : heat capacity [J/g]
C_{WP} : Weisz-Prater parameter, dimensionless
D_t : tube diameter [cm]
E : activation energy [J/mol]
F_{obj} : objective function
ΔH : heat of formation [J/mol]
k : reaction rate constant [mol/kg/s]
K_i^{ad} : adsorption equilibrium constant of i component [1/bar]
NE : number of experimental conditions
NR : number of reactions
O_n : olefin (C_nH_{2n})
P_i : partial pressure of i component [bar]
P_n : paraffin (C_nH_{2n+2})
r_j : rate of reaction j [mol/kg/s]
R_n : alkylidene (C_nH_{2n+1})
U : overall heat transfer coefficient [J/cm^2/s/K]
u_s : linear velocity [cm/s]
v : stoichiometric coefficient
w : weighting factor
z : length of reactor [cm]

Greek Letters

θ : fraction of surface intermediate
ρ_B : bulk density [g/cm^3]
ρ_g : gas density [g/cm^3]

Subscripts

i : species
j : reaction
q : objective

SUPPORTING INFORMATION

Additional information as noted in the text. This information is available via the Internet at http://www.springer.com/chemistry/journal/11814.

REFERENCES

1. A. Y. Khodakov, W. Chu and P. Fongarland, *Chem. Rev.*, **107**, 1692 (2007).
2. B. H. Davis, *Top. Catal.*, **32**, 143 (2005).
3. E. Iglesia, *Appl. Catal. A*, **161**, 59 (1997).
4. M. E. Dry, *Catal. Today*, **71**, 227 (2002).
5. N. Tsubaki, S. Sun and K. Fujimoto, *J. Catal.*, **199**, 236 (2001).
6. S. H. Song, B. S. Lee, J. W. Bae, P. S. Sai Prasad and K. W. Jun, *Catal. Commun.*, **9**, 2282 (2008).
7. M. H. Woo, J. M. Cho, K. W. Jun, Y. J. Lee and J. W. Bae, *ChemCatChem*, **7**, 1460 (2015).
8. S. H. Kwack, M. J. Park, J. W. Bae, S. J. Park, K. S. Ha and K. W. Jun, *Fuel Process. Technol.*, **92**, 2264 (2011).
9. S. J. Park, S. M. Kim, M. H. Woo, J. W. Bae, K. W. Jun and K. S. Ha, *Appl. Catal. A: Gen.*, **419-420**, 148 (2012).
10. B. S. Lee, I. H. Jang, J. W. Bae, S. H. Um, P. J. Yoo, M. J. Park, Y. C. Lee and K. W. Jun, *Catal. Surv. Asia.*, **16**, 121 (2012).
11. S. H. Kwack, J. W. Bae, M. J. Park, S. M. Kim, K. S. Ha and K. W. Jun, *Fuel*, **90**, 1383 (2011).
12. S. H. Kwack, M. J. Park, J. W. Bae, K. S. Ha and K. W. Jun, *Reac. Kinet. Mech. Catal.*, **104**, 483 (2011).
13. G. Yang, D. Gao, J. Zhang, J. Zhang, Z. Shi, Z. Zhu and D. Xue, *RSC Adv.*, **3**, 508 (2013).
14. C. I. Ahn, H. M. Koo, J. M. Cho, H. S. Roh, J. B. Lee, Y. J. Lee, E. J. Jang and J. W. Bae, *Appl. Catal. B: Environ.*, **180**, 139 (2016).
15. H. Zhu, R. Razzaq, L. Jiang and C. Li, *Catal. Commun.*, **23**, 43 (2012).
16. B. A. Sexton, A. E. Hughes and T. W. Turney, *J. Catal.*, **97**, 390 (1986).
17. R. J. Madon and E. Iglesia, *J. Catal.*, **139**, 576 (1993).
18. A. Lapidus, A. Krylova, V. Kazanskii, V. Borovkov, A. Zaitsev, J. Rathousky, A. Zukal and M. Jancalkova, *Appl. Catal. A*, **73**, 65 (1991).
19. K. H. Cats and B. M. Weckhuysen, *ChemCatChem*, **8**, 1531 (2016).
20. C. I. Ahn, H. M. Koo, M. Jin, J. M. Kim, T. G. Kim, Y. W. Suh, K. J. Yoon and J. W. Bae, *Micropor. Mesopor. Mater.*, **188**, 196 (2014).
21. V. Ponec and W. A. van Barneveld, *Ind. Eng. Chem. Prod. Res. Dev.*, **18**, 268 (1979).
22. C. K. Rofer-DePoorter, *Chem. Rev.*, **81**, 447 (1981).
23. K. H. Ernst, E. Schwarz and K. Christmann, *J. Chem. Phys.*, **101**, 5388 (1994).
24. J. T. Kummer, T. W. DeWitt and P. H. Emmett, *J. Am. Chem. Soc.*, **70**, 3632 (1948).
25. E. van Steen and H. Schulz, *Appl. Catal. A.*, **186**, 309 (1999).
26. A. T. Bell, *Catal. Rev. Sci. Eng.*, **23**, 203 (1980).
27. C. S. Kellner and A. T. Bell, *J. Catal.*, **70**, 418 (1981).
28. J. P. Hovi, J. Lahtinen, Z. S. Liu and R. M. Nieminen, *J. Chem. Phys.*, **102**, 7674 (1995).
29. W. A. A. van Barneveld and V. Ponec, *J. Catal.*, **88**, 382 (1984).
30. R. W. Joyner, *Catal. Lett.*, **1**, 307 (1988).
31. H. Schulz, K. Beck and E. Erich, *Fuel. Process. Technol.*, **18**, 293 (1988).
32. C. G. Visconti, E. Tronconi, L. Lietti, R. Zennaro and P. Forzatti, *Chem. Eng. Sci.*, **62**, 5338 (2007).
33. H. J. Jun, M. J. Park, S. C. Baek, J. W. Bae, K. S. Ha and K. W. Jun, *J. Natural Gas Chem.*, **20**, 9 (2011).